Applied Surface Science 611 (2023) 155590

Contents lists available at ScienceDirect

Applied Surface Science

journal homepage: www.elsevier.com/locate/apsusc

Full length article

Surface protonic conductivity in chemisorbed water in porous nanoscopic CeO_2

Xinwei Sun [a], Einar Vøllestad [b], Per Martin Rørvik [b], Sebastian Prodinger [a], Georgios N. Kalantzopoulos [a], Athanasios Chatzitakis [a], Truls Norby [a,*]

[a] Department of Chemistry, University of Oslo, Centre for Materials Science and Nanotechnology (SMN), POB 1126 Blindern, NO-0318 Oslo, Norway
[b] Sustainable Energy Technology, SINTEF Industry, Forskningsveien 1, NO-0373 Oslo, Norway

ARTICLE INFO

Keywords:
Ceria
CeO_2
Porous
Hydrogenation
Water adsorption
Chemisorption
Conductivity
Protonic
Surface
Brick layer model

ABSTRACT

CeO_2 surfaces play decisive roles in heterogeneous catalysis of important processes. Here, we investigate adsorption and dissociation of water and migration of protons on internal surfaces of nanoscopic porous CeO_2. Sorption and thermogravimetry confirm literature suggestions that the surface is hydrogenated to Ce^{3+} ions and protons H^+. The following chemisorption is dissociative, yet weak, and physisorption sets in only at the very highest relative humidities, reflecting hydrophobic behaviour. We link sample conductivities to surface protonic conductances via a brick layer model and show that behaviours at high, intermediate, and low temperatures with, respectively, positive, close to zero, and negative apparent activation energies and $p_{H_2O}^{1/2}$, $p_{H_2O}^{1}$, and $p_{H_2O}^{3/2}$ dependences, can be attributed to different models of migration all within the chemisorbed layer, without contribution from physisorbed water. While CeO_2 may special in this respect due to the effect of the hydrogenated surface, we believe the extended models of transport in the chemisorbed layer may apply also to other oxides. Unsaturated chemisorption may play an important role for CeO_2 as catalyst in that the surface is left available for reactant molecules, still with availability of dissociated and mobile protons in the chemisorbed layer and electronic defects by Ce^{3+} in the surface.

1. Introduction

Ceria (CeO_2) takes on a cubic fluorite structure irrespective of temperature, and is remarkably unreactive with bases and acids such as H_2O and CO_2 and most acidic metal oxides. It has a well-understood defect structure dominated by understoichiometry ($CeO_{2-\delta}$; oxygen vacancies and charge compensating electrons representing Ce^{3+}). Lower-valent acceptor impurities or deliberate doping with for instance Gd^{3+} or Sm^{3+} to form gadolinia- or samaria-doped ceria (GDC, SDC) enhance the concentration of oxygen vacancies and suppress electrons, making the material a good oxide ion conductor for use as a solid-state electrolyte in solid oxide fuel cells (SOFCs). [1,2] The oxygen vacancies in bulk ceria have unfavourable hydration thermodynamics and there is hence no reliable report of significant hydration or proton conductivity in regularly acceptor-doped bulk ceria, and only a hardly measurable hydrogen permeability. [3] It has recently been shown that doping with 50% La^{3+} to form $Ce_{0.5}La_{0.5}O_{1.75}$ (or "$Ce_2La_2O_7$") leads to some hydration, but this is attributed to the affinity of protons to oxide ions fully coordinated by basic La^{3+} ions. [4]

Following discovery of surface protonic conductivity in other MO_2 oxides like undoped ZrO_2 and yttria-stabilized zirconia (YSZ), [5–10] TiO_2, [11–13] and SiO_2, [14] CeO_2 was found to behave similarly. Early reports on nanocrystalline samples attributed the protonic conduction to grain boundary transport, [15–17] but it is now accepted that the triple-grain junctions in some studies were open enough that it can be treated as surface transport in a porous material, and that fully dense materials do not exhibit appreciable protonic conductivity. Porous undoped and acceptor doped CeO_2 exhibits surface protonic conductivity in chemisorbed water down to around 200 °C. Below this, an increase with decreasing temperature is traditionally attributed to conduction in physisorbed water, [18–20] but we shall in the present paper see that it for a large part arises from chemisorbed water alone.

Runnerstrom et al. [21] found that CeO_2 and TiO_2 thin films with grain sizes well below 10 nm exhibit more pronounced protonic conductivity across the minimum at intermediate temperatures (100–350 °C) than more well-crystallised samples. This tendency is

* Corresponding author.
E-mail address: truls.norby@kjemi.uio.no (T. Norby).

https://doi.org/10.1016/j.apsusc.2022.155590
Received 22 June 2022; Received in revised form 15 October 2022; Accepted 2 November 2022
Available online 8 November 2022

observed also for certain facets of surfaces on TiO_2 [22] and for poorly crystallised ZrO_2. [23] Dependences on oxygen activity and morphology led the authors to suggest that oxygen vacancies promote dissociative adsorption of water and resulting higher protonic conductivity. Simons et al. [24] studied CeO_2 thin films and concluded that hydration is a slow process, while adsorption along surfaces and through open pores is fast. This may explain the inconsistency on the protonic conductivity of porous and dense ceria in literature.

Based on measurements of conductivity of dense films and porous ceramic samples of CeO_2 under wet and dry atmospheres, Gregori et al. [20] considered that protons from adsorbed water may dissociate and migrate in the subsurface region as well as in the layer of adsorbed water. They proposed a brick-layer model (BLM) for a qualitative estimate of the conductivity of oxides with small amounts of open porosity based on the conductivity and thickness of the water layer and the size and volume fraction of pores. In their assessment, they assume that the dissociation into charge carriers follows autoprotolysis of water, and based on the measured sample conductivity and their BLM, they found that mobilities of protons in the adsorbed water layers are within order of magnitude of that in bulk water at 200 °C.

An important application of nano- or microcrystalline ceria is as catalyst or support for noble metal nanoparticles in chemical industry and combustion engine exhaust catalyst systems. [25] Its catalytic activity suggests that CeO_2 surfaces deviate from the simplicity of bulk cubic CeO_2. [26,27] This may comprise enhanced understoichiometry and n-type conductivity as well as hydration. On-going density functional theory (DFT) calculations show strong tendency of hydration of reduced CeO_2 surfaces, meaning that the surfaces may be seen as reduced oxyhydroxides, formed according to schematic hydrogenation reactions like

$$CeO_2 + \frac{1}{2}H_2O(g) \rightleftarrows CeOOH + \frac{1}{4}O_2(g) \quad (1)$$

$$CeO_2 + \frac{1}{2}H_2(g) \rightleftarrows CeOOH \quad (2)$$

This is supported by in situ electron energy loss spectroscopy (EELS) of CeO_2 nanoparticles in transition electron microscopy (TEM) showing that Ce^{3+} in a surface layer oxidises to Ce^{4+} during heating in vacuum, which we may assign to dehydrogenation (Eq. (2) reversed). [28]

While the surface chemistry of CeO_2 is important and much studied, [29,30] the adsorption of water and resulting surface protonic transport are far from well understood. Here we contribute a study of adsorption of water and dissociation and migration of protons in chemisorbed and physisorbed water on the internal surfaces of nanoscopic porous CeO_2 ceramics. The results are interpreted in terms of a theoretical framework that relates adsorption thermodynamics via transport theory to surface conductance, and a brick layer model that quantitatively relates surface conductance with the measured conductivity of highly porous materials. [23] The combined used of thermogravimetry and conductivity vs T and p_{H_2O} suggests that hydrogenation of the surface must be taken into account and that transport in the chemisorbed layer covers a wider range of temperature than hitherto realised, with an extended set of models for this. Physisorption is suppressed due to the hydrophobicity of CeO_2 that, in turn, arises from the hydrogenated surface.

2. Experimental

2.1. Materials and preparation

Ceria nanopowder (< 50 nm particle size, 99.95% trace rare earth metals basis, SKU no. 700290, Sigma Aldrich) was cold-pressed at ~65 MPa, followed by sintering at 550 or 750 °C in air with a dwell time of 8 h into disks with approximate dimensions of 20 mm diameter and 2 mm thickness. The sintered samples are hereafter denoted CeO_2–550 and CeO_2–750. The resulting relative densities of the disks were about 50% (CeO_2–550) and 62% (CeO_2–750), calculated from their mass and geometry and nominal density of stoichiometric CeO_2 of 7.22 g cm^{-3}. [31]

2.2. Characterization

The microstructure and porosity of the samples were analysed by scanning electron microscopy (SEM, Hitachi SU8230). Powder X-ray diffraction with a Bruker D8 Discover diffractometer with CuKα_1 radiation (λ = 1.5406 Å, Bragg-Brentano mode) was used to verify the structure and examine the crystallite size.

Nitrogen sorption measurements were performed on a BELSORP mini II instrument (MicrotracBEL Corp., Japan) at 77 K to determine the specific surface area (*SSA*), and the pore size distribution of the materials. In each experiment, approximately 200 mg of material was weighed into a quartz cell. The samples were pre-treated by annealing under dynamic vacuum for 2 h at 150 °C. The total *SSA* was extracted from the nitrogen adsorption isotherms via the Brunauer–Emmett–Teller (BET) method. [32] Non-local density functional theory (NLDFT) calculations of the pore size distribution were performed using the commercial BELMaster software (MicrotracBEL Corp., Japan). The Grand Canonical Monte Carlo (GCMC) calculation method was applied on the adsorption branch using the nitrogen physisorption data collected at 77 K, assuming a slit pore model.

Water sorption measurements were performed at 25 °C using a BELSORP Max physisorption instrument (MicrotracBEL Corp., Japan) to determine the maximum water capacity. [33] The measurements took place in the relative humidity (*RH*) range: $0 < RH = \frac{p_{H_2O}}{p_{ce}} < 0.9$, with p_{ce} being the condensation equilibrium partial pressure of H_2O at 25 °C. In each experiment, approximately 200 mg of material was weighed into a quartz cell and pre-treated with annealing under dynamic vacuum for 2 h at 150 °C in situ to avoid exposure to atmospheric humidity. The number of physisorbed H_2O molecules per unit surface is calculated from Eq. (3), where wt% is the gravimetric adsorption, N_A is Avogadro's number, MW_{gas} is the molecular weight of the adsorbed gas (H_2O), and SSA_g is the gravimetric specific surface area from BET analysis.

$$\frac{N_{molecule}}{nm^2} = \frac{N_A \cdot wt.\%}{10^{20} \cdot MW_{gas} \cdot SSA_g} \quad (3)$$

Thermogravimetry (TG) was carried out using a 449 F1 Jupiter® thermal analyser (Netzsch GmbH, Germany) on the pristine CeO_2 powder and sintered samples under bottle-dry or wet N_2 (99.999%) purge gases. The sintered samples were crushed coarsely to fit into the sample holder, while retaining its microstructure. The samples were heated to 550 °C at 3 K min^{-1} in bottle-dry N_2 at a flow rate of 40 mL min^{-1}, thereafter held at the given temperature for at least 2 h to eliminate adsorbed water and organic residue from the sample surface. The p_{H_2O} dependence of water adsorption was measured at 400, 100, 50 and 30 °C, while the temperature dependence was conducted as follows: After fully dehydrating at 550 °C as described above, the samples were equilibrated at 550 °C at p_{H_2O}= 0.020 atm and measured during stepwise cooling to 25 °C – the weight increase reflects the total content of hydrogen as well as both chemisorbed and physisorbed water. Background measurements in bottle-dry N_2 were carried out under otherwise identical conditions and used for background subtraction, with the dry-to-wet step at 550 °C as a starting point, assuming that uptakes from water in dry atmosphere at 550 °C is zero.

For electrical characterization, symmetrical circular Ag paste electrodes of 10 mm diameter were painted on both faces of the sintered pellets. Electrical conductivity was measured via Pt mesh and four Pt wire contacts by electrochemical impedance spectroscopy (EIS) in a ProboStat™ sample holder cell (NORECS, Norway). The atmosphere was a flow of bottle-dry or wet (p_{H_2O}= 0.025 atm) N_2 (99.999%), O_2 (99.5% or 99.999%) or air, or N_2 with variable p_{H_2O} controlled by a HumiStat gas-mixer and humidifier (NORECS, Norway). Impedance spectra (10 MHz – 10 mHz, 100–500 mV RMS) were recorded using a

Novocontrol alpha-A spectrometer coupled with a ZG4 interface. Impedance data were analysed and modelled with ZView™ software (Scribner Associates Inc.). Specific conductivities of the porous samples were calculated based on their thickness and electrode area, without correction for the porosity.

3. Results and discussion

3.1. Microstructural characterization

Fig. 1 presents SEM images of the CeO_2–550 and CeO_2–750 samples, showing average grain sizes of approximately 40 and 90 nm, respectively. The shape of the particles of the CeO_2–550 sample remains rounded, similar to the pristine powder, but evolved to more faceted surfaces upon sintering at 750 °C. X-ray diffractograms (SI 2.1, Fig. S1) of the CeO_2 starting powder and the sintered samples show cubic fluorite structure with space group *Fm*-3*m* and lattice parameters $a = b = c =$ 5.411 Å (COD_9009008). The grain sizes obtained from Scherrer analysis were 21 and 62 nm for CeO_2–550 and CeO_2–750, respectively, while they were 20 and 80 nm from Rietveld analysis, in rough agreement with those from SEM images, which we have used in subsequent quantitative analyses. From weight and geometry, sintering at 550 and 750 °C resulted in relative densities of around 50 and 62%, respectively, in agreement with the SEM images.

3.2. Nitrogen and water sorption measurements

N_2 adsorption-desorption of all CeO_2 samples display characteristic type II isotherms (SI 2.2, Fig. S3a). [34] BET analyses of the pristine CeO_2, CeO_2–550, and CeO_2–750 provide gravimetric specific surface area (SSA_g) of $3.2\bullet10^5$, $3.1\bullet10^5$ and $5.9\bullet10^4$ $cm^2\ g^{-1}$, respectively, (Table 1) and average pore size of 13, 14, and 20 nm (SI 2.2, Fig. S3b), which is again characteristic of mesoporous structures. The volume specific surface area (SSA_v) is also included in Table 1, calculated as the product of the SSA_g and the density of the porous sample. The results reflect the modest increases in grain size and relative density by sintering at 750 °C vs 550 °C, while the surface area for adsorption varies by a factor of 5, probably due to elimination of sub-granular and surface defects.

Water sorption measurements were performed at 25 °C for all samples, exhibiting type II isotherms similar to the N_2 adsorption. The number of adsorbed H_2O molecules normalised for BET surface area via Eq. (3) is shown in Fig. 2 at $0 < RH < 0.9$ and is remarkably equal for all three samples. The surface coverage is also shown, on basis of 5 H_2O per nm^2 as monolayer coverage. [35] A first layer of chemisorbed water appears to be in place already at low *RH* in agreement with calorimetric adsorption measurements on various oxides. [35–37] However, saturation appears to be reached only at closer to two monolayers. As indicated by TG results later on, part of this may reflect subsurface hydrogenation that gives an overestimate of what is interpreted as chemisorbed water.

The double-logarithmic insert in Fig. 2 displays a slope around 1/3 at low *RH*. This shows that adsorption is far from molecular (slope of 1) and instead suggests that each water molecule dissociates into 2, 3, or 4 species (slopes of ½, 1/3, or ¼, respectively). Based on the TG results to follow, we believe this reflects a combination of subsurface hydrogenation to protons and electrons with a $p_{H_2O}^{1/4}$ dependence and dissociative chemisorption with a $p_{H_2O}^{1/2}$ dependence.

Fig. 2 further shows that major uptake of physisorbed water beyond the chemisorbed layer occurs in our material only at unusually high *RH*, reflecting stronger adsorbate-adsorbate (H_2O-H_2O) interaction than adsorbate-adsorbent (H_2O-CeO_2) interaction. The α parameter (*RH* at which we reach half of the total water capacity, taken here to be at $RH = 0.9$) is a qualitative indication of surface hydrophobicity. [38] It was extracted from the water sorption data and listed in Table 1 and show that all CeO_2 samples can be considered as hydrophobic by having high α values of 0.78–0.82. Hydrophobicity is demonstrated for low-index CeO_2 surfaces by DFT calculations. [39] The intrinsic hydrophobicity of CeO_2 surfaces is a property it has in common with other rare earth (*RE*) oxides RE_2O_3. [40] We note that this may be connected with the general stability of *RE*OOH oxyhydroxides and hence tendency of RE_2O_3 forming a *RE*OOH-like surface by hydration, like CeO_2 may form CeOOH by hydrogenation.

The total volume of water adsorbed at *RH* of 0.9, commonly taken as the water adsorption capacity, can serve as a measure of sample porosity. [41] As seen in Table 1, it is indeed proportional to the BET surface area. The results indicate that at a *RH* of 0.9 there will be around 10 monolayers of water with a total thickness of close to 3 nm based on a monolayer thickness of 2.82 Å. [42]

3.3. Thermogravimetry (TG)

Fig. 3 shows isothermal p_{H_2O} dependences of water uptake measured by TG. If in Fig. 3 (a) we attribute the weight increase at 400 °C to H_2O, the water layer is still far from being complete assuming a monolayer coverage as 5 H_2O per nm^2 as mentioned above. A close to a $p_{H_2O}^{1/4}$ dependence is observed for both samples at 400 °C. Our recent STEM-EELS study [28] suggests that CeO_2 surfaces have a CeOOH-like layer according to Eq. (1) or Eq. (2), in agreement with other findings of Ce^{3+} in CeO_2 nanoparticles. [36,43] The TG results at 400 °C may then be better interpreted in terms of weight of uptake of H_2 instead of H_2O. Although it is reasonable per se and from the TEM-EELS study that the hydrogen is dissolved in the subsurface, we may still express the uptake as a surface concentration, i.e., number of H_2 per nm^2 surface (filled symbols in the figure). In defect-chemical terms the hydrogenation of the subsurface CeO_2 can be written

$$Ce_{Ce}^{x} + O_O^x + \frac{1}{2}H_2O(g) \rightleftarrows Ce_{Ce}^{/} + OH_O^{\bullet} + \frac{1}{4}O_2(g) \quad (4)$$

where Ce_{Ce}^{x} and $Ce_{Ce}^{/}$ represent Ce^{4+} and Ce^{3+}, respectively, and O_O^x and $OH_O^{\bullet}$ represent oxide and hydroxide ions, respectively. If this reaction

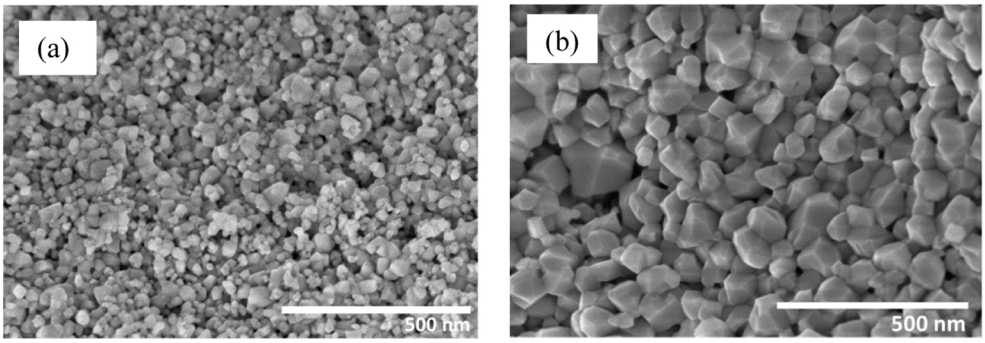

Fig. 1. SEM images of the (a) CeO_2–550 and (b) CeO_2–750 samples.

Table 1
Sorption parameters from N_2 adsorption isotherms at 77 K and water adsorption data at 298 K.

Samples	Specific surface area[§] (*SSA*)		Total pore volume[§] (cm^3 g^{-1})	Average pore size (BJH)[§] (nm)	α (*RH* at 50% of H_2O uptake at RH = 0.9)	Water capacity[§§] (cm^3 g^{-1})
	SSA_g (cm^2 g^{-1})	SSA_v (cm^2 cm^{-3})				
Pristine CeO_2	$3.2•10^5$	n.a.	$1.1•10^{-1}$	13	0.78	53
CeO_2–550	$3.1•10^5$	$1.1•10^6$	$1.0•10^{-1}$	14	0.79	55
CeO_2–750	$5.9•10^4$	$2.6•10^5$	$3.5•10^{-2}$	20	0.82	10

[§] Estimated from N_2 adsorption isotherms at 77 K.
[§§] From H_2O adsorption data at 298 K at $RH = 0.9$.

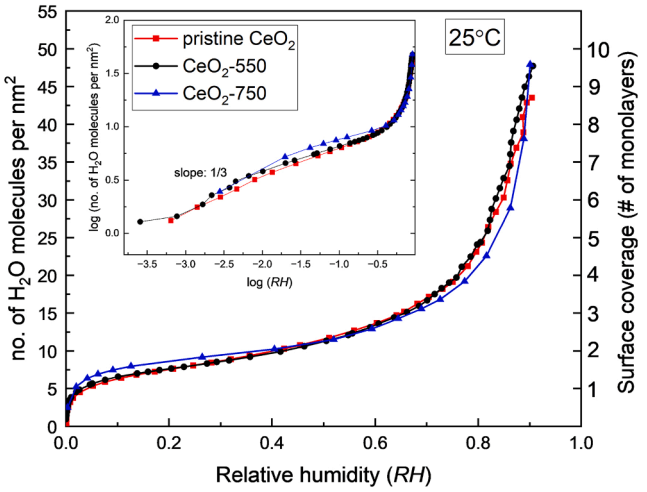

Fig. 2. Number of adsorbed water molecules per nm^2 as a function of relative humidity (*RH*) calculated from water sorption isotherms at 25 °C. The right-hand axis shows the same data in number of layers of water, assuming a monolayer coverage of 5 H_2O per nm^2. The inset shows a double-logarithmic plot of the data, suggesting approximately a $p_{H_2O}^{1/3}$ dependence in the low *RH* part.

provides the dominant charged defects, but at low concentrations, we obtain

$$\left[OH_O^{\bullet}\right] = \left[Ce_{Ce}^{/}\right] = K_H^{1/4} p_{H_2O}^{1/4} p_{O_2}^{-1/8} \quad (5)$$

where K_H is the equilibrium coefficient of the reaction. The qualitative fit with the observed $p_{H_2O}^{1/4}$ dependence supports our suggestion that the weight increase at 400 °C is dominated by reduction of the subsurface, and not by adsorption of water.

Fig. 3 (b) shows the p_{H_2O} dependence of water uptake at 100, 50, and 30 °C, see also Fig. S4 in SI 3 for more detail on slopes and reversibility at 100 and 30 °C. At 100 °C, the weight change represents filling up of a yet far from complete chemisorbed water layer, with an overall $p_{H_2O}^{1/2}$ dependence – showing that the chemisorption is mainly dissociative. At 50 °C and 30 °C, the lower p_{H_2O} dependence may represent a beginning completion of the chemisorbed layer, while physisorbed water comes on at the highest p_{H_2O} at 30 °C ($RH > 50\%$), giving rise to what appears to approach a $p_{H_2O}^{1}$ dependence (molecular physisorption).

As a thermodynamic basis for the p_{H_2O} dependences and later on enthalpies of TG data and models for conduction to follow, we apply an extension of a recently proposed framework and Kröger-Vink type notation for surface reactions and transport on ZrO_2 [23] (see SI for details). We first write the molecular chemisorption to a surface cation,

$$M_{M_s}^{x} + H_2O(g) \rightleftharpoons M_{M_s}OH_2^{x} \quad (6)$$

where *M* denotes the cation in binary oxides, in this case $M = Ce$ and surface cation and oxide ion sites are denoted M_s and O_s. The

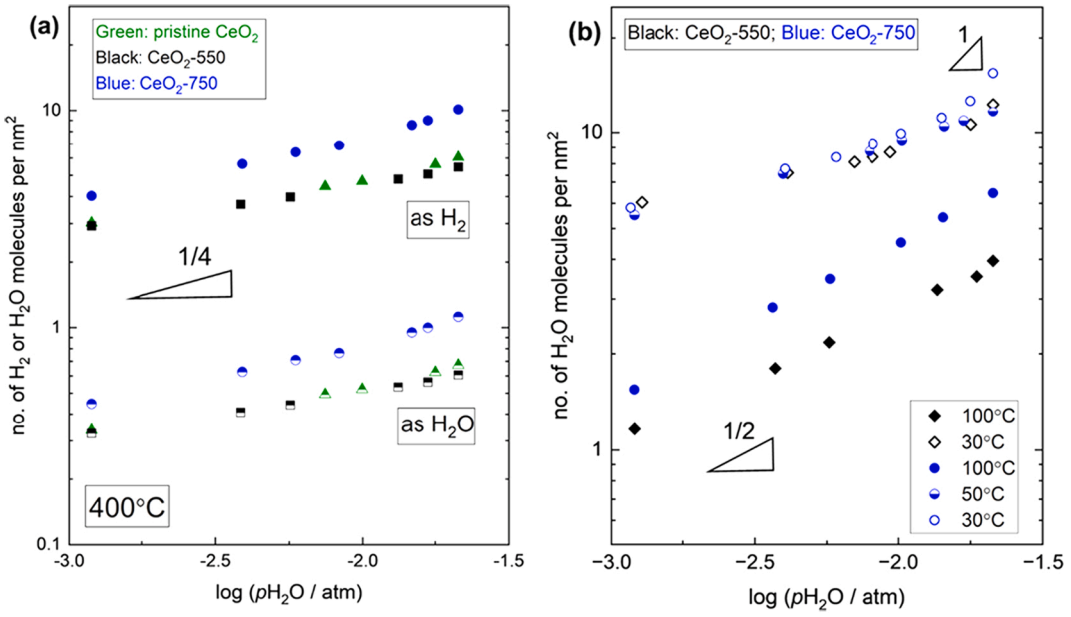

Fig. 3. Area specific adsorption in CeO_2 samples as a function ofp_{H_2O} in N_2 represented as number of H_2 or H_2O per nm^2 measured at (a) 400 °C and at (b) 100, 50, and 30 °C.

corresponding equilibrium coefficient $K_{a_{cm}}$ can be written

$$K_{a_{cm}} = \frac{X_{M_{M_s}OH_2^x}}{X_{M_{M_s}^x}\frac{p_{H_2O}}{p^0}} = \frac{\gamma_{M_{M_s}OH_2^x}}{\gamma_{M_{M_s}^x}\frac{p_{H_2O}}{p^0}} = exp\left(\frac{\Delta S^0_{a_{cm}}}{R}\right)exp\left(\frac{-\Delta H^0_{a_{cm}}}{RT}\right) \quad (7)$$

where X denotes site fraction and γ denotes surface concentration. For low coverage, this yields

$$\gamma_{M_{M_s}OH_2^x} = \gamma_{M_s}\frac{p_{H_2O}}{p^0}K_{a_{cm}} = \gamma_{M_s}\frac{p_{H_2O}}{p^0}exp\left(\frac{\Delta S^0_{a_{cm}}}{R}\right)exp\left(\frac{-\Delta H^0_{a_{cm}}}{RT}\right) \quad (8)$$

Dissociation of a proton to a surface oxide ion is similarly written

$$M_{M_s}OH_2^x + O^x_{O_s} \rightleftharpoons M_{M_s}OH^{/} + OH^{\bullet}_{O_s} \quad (9)$$

with equilibrium coefficient

$$K_{d_{cs}} = \frac{\gamma_{M_{M_s}OH^{/}}\gamma_{OH^{\bullet}_{O_s}}}{\gamma_{M_{M_s}OH_2^x}\gamma_{O^x_{O_s}}} = exp\left(\frac{\Delta S^0_{d_{cs}}}{R}\right)exp\left(\frac{-\Delta H^0_{d_{cs}}}{RT}\right) \quad (10)$$

The sum of both reactions describes dissociative chemisorption,

$$M^x_{M_s} + O^x_{O_s} + H_2O(g) \rightleftharpoons M_{M_s}OH^{/} + OH^{\bullet}_{O_s} \quad (11)$$

with equilibrium coefficient

$$K_{a_{cds}} = K_{a_{cm}}K_{d_{cs}} = \frac{\gamma_{M_{M_s}OH^{/}}\gamma_{OH^{\bullet}_{O_s}}}{\gamma_{M_{M_s}}\gamma_{O^x_{O_s}}\frac{p_{H_2O}}{p^0}} = exp\left(\frac{\Delta S^0_{a_{cds}}}{R}\right)exp\left(\frac{-\Delta H^0_{a_{cds}}}{RT}\right) \quad (12)$$

where the standard entropy and enthalpy changes $\Delta S_{a_{cds}}{}^0$ and $\Delta H_{a_{cds}}{}^0$ are sums of those for molecular chemisorption and dissociation. The electroneutrality is

$$\gamma_{M_{M_s}OH^{/}} = \gamma_{OH^{\bullet}_{O_s}} \quad (13)$$

and insertion into Eq. (12) yields the observed $p_{H_2O}^{1/2}$ dependence of the dissociated species:

$$\gamma_{OH^{\bullet}_{O_s}} = \gamma_{M_{M_s}OH^{/}} = \sqrt{K_{a_{cds}}\gamma_{M_{M_s}}\gamma_{O^x_{O_s}}\frac{p_{H_2O}}{p^0}} = \sqrt{\gamma_{M_{M_s}}\gamma_{O^x_{O_s}}\frac{p_{H_2O}}{p^0}}exp\left(\frac{\Delta S^0_{a_{cds}}}{2R}\right)exp\left(\frac{-\Delta H^0_{a_{cds}}}{2RT}\right) \quad (14)$$

If chemisorbed water remains undissociated, the mass gain would show a $p_{H_2O}^{1}$ dependence (Eq. (8)) while if it is predominantly dissociated, we obtain a $p_{H_2O}^{1/2}$ dependence (Eq. (14)). If the overall process saturates at complete coverage, the mass of the chemisorbed layer will become constant, independent of p_{H_2O}, irrespective of the degree of dissociation.

The mass gain as a function of temperature in wet atmosphere and interpreted as adsorption of water is shown in SI 3, Fig. S5. Fig. 4 displays the same data in area-specific terms, obtained by using the SSA_g from BET analysis. The mass gain upon cooling from 550 °C appears to level off towards 200 °C corresponding to around 0.8 H_2O per nm^2 for the pristine CeO_2 powder and the CeO_2–550 sample and around 2 H_2O per nm^2 for CeO_2–750. Such low coverage supports the finding that what we see in this region is not chemisorption of water, but saturation of the CeOOH-like subsurface layer as a result of hydrogenation of CeO_2 from water vapour. Recalculated, the apparent levels of 0.8 and 2 H_2O per nm^2 correspond then instead to 7 and 18 H_2 (or 14 and 36H) per nm^2, meaning that the layer of "CeOOH" with Ce^{3+} and H^+ goes 4–8 unit cells down if each Ce takes one electron.

The stronger increase in water adsorption below 200 °C then reflects chemisorbed water. After subtraction of the mass from the CeOOH-like layer, the data in the range 200–100 °C have enthalpies around −40 kJ mol^{-1}. If this is molecular chemisorption, we expect from Eq. (8) an enthalpy corresponding to $\Delta H_{a_{cm}}{}^0$. The p_{H_2O} dependences suggested predominantly dissociative chemisorption, and following Eq. (14) the

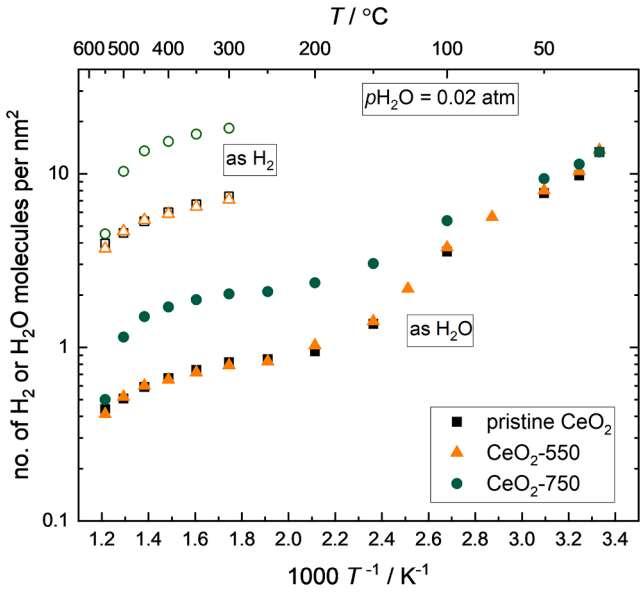

Fig. 4. Area-specific uptake from water by TG interpreted as number of H_2 or H_2O per nm^2 for the CeO_2 samples in the range 550–25 °C in wet (p_{H_2O}= 0.02 atm) N_2 atmosphere.

enthalpy is then instead $\frac{1}{2}\Delta H^0_{a_{cds}} = \frac{1}{2}\left(\Delta H^0_{a_{cm}} + \Delta H^0_{d_{cs}}\right)$. Existing literature suggests that $\Delta H_{a_{cm}}{}^0 = -60$ kJ mol^{-1} based on calorimetry [36] and first-principles calculations [44,45], and we may take $\Delta H_{d_{cs}}{}^0 \approx 20$ kJ mol^{-1} as a round-off estimate based on the dissociation enthalpy 22 kJ mol^{-1} of water adsorbed on YSZ [46]. We hence expect enthalpies of $\Delta H_{a_{cds}}{}^0 \approx -20$ kJ mol^{-1} for the dissociated case, changing towards $\Delta H_{a_{cm}}{}^0 \approx -60$ kJ mol^{-1} as it turns molecular with decreasing T and increasing p_{H_2O}. For now we observe that the experimental enthalpies lie in a range in between, but they are not sufficient for deeper analysis.

Towards 50 °C, the curves in Fig. 4 display a tendency of levelling out at around 10 H_2O per nm^2, in agreement with the curve at the same temperature in Fig. 3 (b), which we attribute to saturation at full coverage of the chemisorbed layer. On further approach to RT and the highest *RH*, there is a new increase in mass gain as physisorbed water comes on, visible in both Fig. 3 (b) and Fig. 4.

3.4. Electrical conductivity

3.4.1. Impedance spectroscopy

Examples of impedance spectra are shown in SI 4.1 Fig. S6. Two overlapping arcs are revealed in the high-frequency range irrespective of sample, temperature and atmospheres (dry/wet), with capacitances in the range of geometric volume dielectrics. Similar duality has been reported for porous YSZ, but with bigger differences in capacitance, suggested to reflect *intra-grain* protonic transport over grain surfaces affiliated with low capacitance and *inter-grain* protonic transport over resistive grain boundaries affiliated with higher capacitance. [6] The present results for CeO_2 are instead similar to what is reported for porous undoped monoclinic ZrO_2, [23] and are suggested to reflect an inherent frequency response of porous ceramic materials with conduction over the concave (neck) and convex (grain) parts of the curved surfaces, now with the grain capacitance being the bigger because of its dielectric solid phase as compared to the concave neck having the smaller capacitance of the gas phase. In the following, we report the conductivity calculated from the sum of the two resistances extracted from the two high frequency responses.

3.4.2. Effects of atmosphere and temperature

The conductivities of CeO_2–550 and CeO_2–750 have been measured

vs temperature below their sintering temperatures. The main features of the electrical conductivity involve native non-protonic conductivity at the highest temperatures and surface protonic conductivity in adsorbed water with characteristic temperature dependences. Like most others studying surface protonics of CeO_2, we observe slow, and sometimes hysteretic changes and equilibria, the most important being irreversible effects of atmosphere (O_2 or air vs N_2), hysteretic adsorption and desorption of water, and what is believed to be surface restructuring and hydrophobicity of water adsorption at near ambient temperatures and high relative humidities. We note that some of these effects may be attributable to changes in the "CeOOH"-like subsurface layer, which only requires transport of protons and electrons and may take place at low temperatures. The observations are detailed in SI 4.2, while we here proceed to report and interpret results taken with long equilibration times under N_2 atmospheres, which represent the most reproducible and systematic behaviours.

3.4.3. *Temperature dependences*

Fig. 5 shows the Arrhenius plots of the conductivity (σ) of both CeO_2 samples, measured in bottle-dry and wet (p_{H_2O}= 0.025 atm) N_2. Under nominally dry conditions, the conductivity is significant and measurable only at the highest temperatures. It follows Arrhenius behaviour, with apparent activation enthalpies of around 80 kJ mol^{-1}. This is low compared to that of the conductivity of many bulk and porous nanoceria materials attributed to oxide ion conduction, [20,24,47] but comparable to what is expected for n-type electronic conduction of CeO_2 [19] (e.g. 0.77 eV for nanocrystalline CeO_2 thin film [21]). Knauth et al. [48] measured the p_{O_2} dependence of conductance of CeO_2 nanopowder and of coarsened powder, which gave rise to a $p_{O_2}{}^{-1/6}$dependence, similar to those of pulsed laser deposition (PLD) thin films. [49] In our work, the lack of an electrode impedance in impedance spectra at high temperatures in dry atmospheres correspondingly suggest that this conduction is electronic (assumingly n-type), and the presence of dual time constants in impedance spectra suggests that it is surface conduction.

The conductivity in wet atmospheres is higher than in dry. Fig. 6 shows the conductivity of our CeO_2 samples after subtraction of the native apparently electronic conductivity measured in dry atmosphere. At temperatures above 500 °C this may be attributed to electrons in the hydrogenated (CeOOH-like) layer, with a high activation energy. This deserves further study, but is beyond the scope of this article.

Below 500 °C, the impedance spectra show – as said above – that we have increasingly dominant surface protonic conduction, with a contribution with positive apparent activation enthalpy attributed to transport in the chemisorbed layer in the range 500–300 °C. In the temperature range 300–200 °C, the conductivity levels out, like in previous studies on nanocrystalline CeO_2 [19,50] formerly not having a plausible interpretation.

Below 200 °C, the conductivity increases with decreasing temperature, while as temperature passes below 100 °C and *RH* surpasses ~6%, the conductivity increases less steeply. These have commonly been attributed to solid- and liquid-like physisorbed water. The TG results showed however that the low-temperature (high *RH*) regions may need re-interpretation in the case of CeO_2: The region 200–100 °C is in fact mainly filling up with chemisorbed water, the first (solid-like) physisorbed water comes on only well below 100 °C, and liquid-like physisorbed water maybe never contributes much to conduction on CeO_2 surfaces due to their hydrophobicity. In the following, we evaluate these assessments by comparing their p_{H_2O} dependences, temperature dependences (enthalpies) and preexponentials with credible models. These partly coincide with and partly go beyond those presented in our preceding work on ZrO_2. [23]

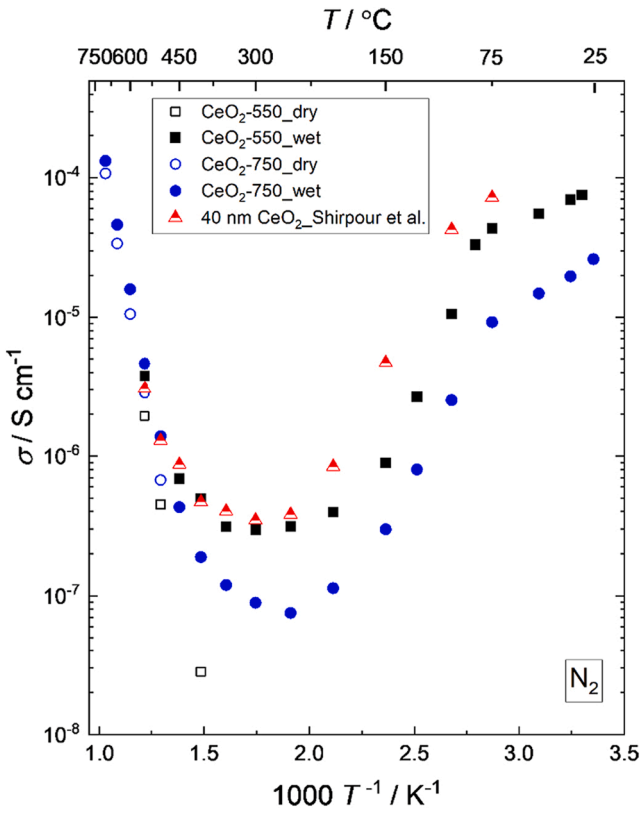

Fig. 5. Plot of σ vs $1/T$ for CeO_2–550 and CeO_2–750 in dry (open symbols) and wet (p_{H_2O} = 0.025 atm, solid symbols) N_2. Protonic conductivity reported by Shirpour et al. [19] for nanocrystalline undoped CeO_2 is shown for comparison.

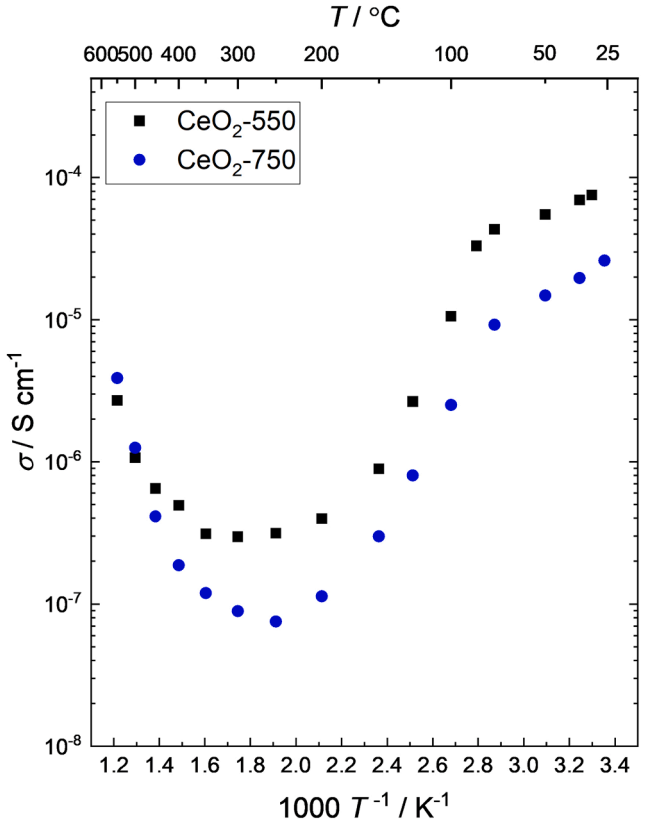

Fig. 6. Plot of σ vs $1/T$ for surface protonic conductivity of CeO_2–550 and CeO_2–750 obtained from wet N_2 atmosphere after subtraction of the dry conductivity.

3.4.4. Isothermal conductivity vs pH_2O

Fig. 7 shows the isothermal p_{H_2O} dependences of the surface protonic conductivity of the two CeO_2 samples. At 400 °C, we have close to a $p_{H_2O}^{1/2}$ dependence of surface protonic conductivity, steepening a bit towards a slope of 1 towards the highest pressure (0.025 atm), coinciding with a report by Manabe et al. [51] of a $p_{H_2O}^{1}$ dependence in the range p_{H_2O}= 0.026–0.2 atm of conductivity over grain surfaces (σ_{intra}) in porous CeO_2 at 400 °C. Studies of $Zr_{1-x}Y_xO_{2-x/2}$ (x = 0.04, 4YSZ) showed a $p_{H_2O}^{1/2}$ dependence of surface protonic conductivity at 400–250 °C, [52] and so did $Ce_{0.9}Gd_{0.1}O_{2-\delta}$ at 200 °C, [53] and $La_2Ce_2O_7$ at 550–250 °C. [54] The $p_{H_2O}^{1/2}$ dependence shows that each adsorbed H_2O molecule splits in two charged species to facilitate protonic transport in chemisorbed water.

At 100 °C, Fig. 7 (b) shows higher slopes reflecting close to $p_{H_2O}^{3/2}$ dependences of conductivity, suggesting involvement of multiple H_2O molecules in the protonic transport step. In our recent report on ZrO_2, [23] we proposed models for surface protonic conduction in the first physisorbed layer with $p_{H_2O}^{3/2}$ and $p_{H_2O}^{2}$ dependences, but based on the TG results for CeO_2 here, we have only chemisorption under these conditions, and we shall derive and parameterise extended models for conductance in the chemisorbed layer that yield similar predictions.

3.5. Modelling the surface protonic conductivity

3.5.1. General expressions of sample conductivity and surface conductance

We now move on to evaluate and parameterise the surface protonic conductivities according to the framework laid down in our work on ZrO_2, [23] expanded and detailed for the present results on CeO_2 in SI 5 (also containing an updated list of abbreviations in SI 1). For this purpose, we first relate the measured conductivity of the porous sample and the conductance of the adsorbed water layer via a brick layer model (BLM, see SI 5.2):

$$\sigma_{M,s,H^+} = \sigma_{M,s,H^+\,0}\frac{1}{T}exp\left(\frac{-\Delta H_c}{RT}\right) = \psi G_{s,H^+\,0}\frac{1}{T}exp\left(\frac{-\Delta H_c}{RT}\right)$$
$$= \psi G^0_{s,H^+0}\left(\frac{p_{H_2O}}{p_0}\right)^n\frac{1}{T}exp\left(\frac{-\Delta H_c}{RT}\right) \quad (15)$$

where $\sigma_{M,\,s,\,H^+}$ in S/cm is the measured surface protonic conductivity of the porous material, $\sigma_{M,\,s,\,H^+\,0}$ in SK/cm is its preexponential factor, ΔH_c is the enthalpy of conductivity, ψ in 1/cm is the factor derived from the BLM connecting $\sigma_{M,\,s,\,H^+}$ and $\sigma_{M,\,s,\,H^+\,0}$ to surface conductance $G_{s,\,H^+}$ in S and its preexponential factor $G_{s,\,H^+\,0}$ in SK. Furthermore, while $G_{s,\,H^+\,0}$ is usually proportional to $p_{H_2O}^{n}$ with n depending on predominant mechanism of adsorption, dissociation, and transport, the factor $G_{s,\,H^+}{}^{0}{}_{0}$ standardises this to $p_{H_2O} = p^0 = 1$ bar.

Fig. 8 shows the geometry-corrected surface protonic conductances $G_{s,\,H^+}$ according to the BLM. They become roughly identical for the two samples over the entire temperature range (see also SI 5.2), demonstrating that the level of the surface protonic conductivity in Fig. 6 is largely determined by the grain size and porosity that enter into the BLM.

The surface conductance in wet atmosphere at the highest temperatures (above 500 °C in Fig. 8) cannot be reasonably modelled with transport in chemisorbed water and we attribute it as said before to transport of protons and/or electrons in the surface and/or subsurface caused by hydrogenation to protons in OH^- groups and electrons as Ce^{3+} in the CeOOH-like layer. An interpretation of its basis including temperature dependence deserves dedicated studies beyond the scope of this paper.

3.5.2. Models and parameterisation of surface conductance in chemisorbed water

The entire temperature dependence of surface protonic conductance can now be depicted by different models derived for adsorption, dissociation, and proton migration in chemisorbed water. A complete treatment of models is provided in SI section 5.3, which also provides schematic illustrations of all cases. Derived p_{H_2O} dependences and estimated preexponentials and activation enthalpies of surface conductance are collected in Table S4. Here we use excerpts to describe and parameterise models that fit the experimental data of Fig. 7 and Fig. 8.

It must be emphasised that the derivation at this stage neglects the possible effects of the surface being more like CeOOH than CeO_2. We treat the mean surface as having 2 oxide ions per Ce ion. The effect of having just one available unprotonated oxide ion for protonation and migration per cerium ion will for the most part be minor, but the parameterisation of models may unavoidably reflect CeOOH-like rather than CeO_2 surfaces in our work like in any other. We see our work hence not as the final, but an important step towards a complete description of

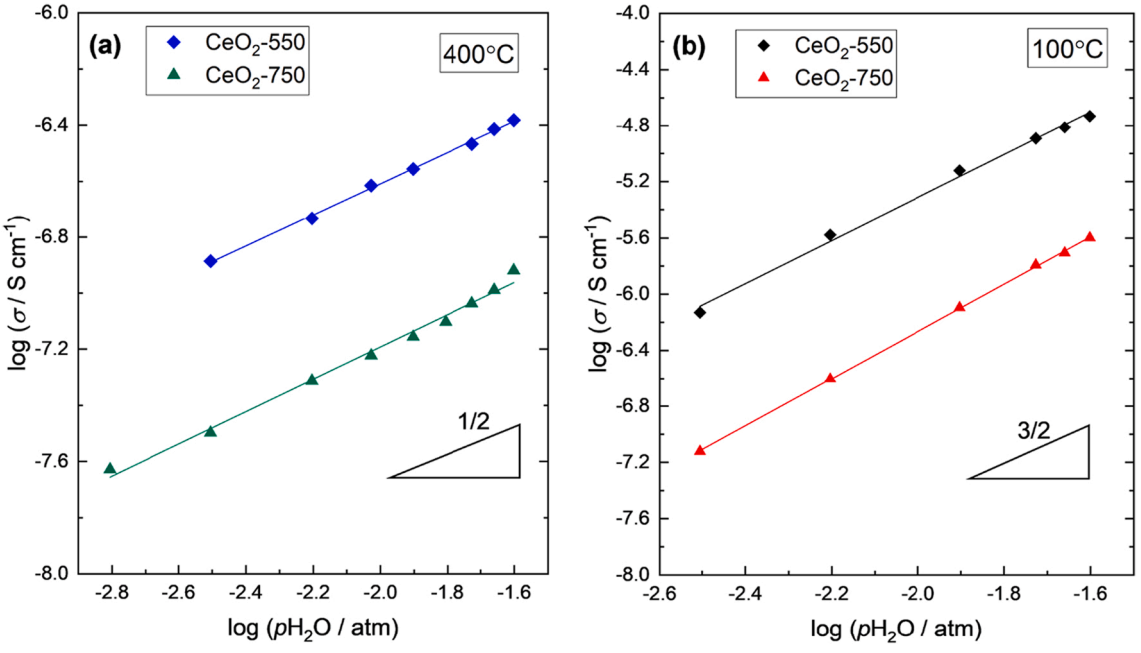

Fig. 7. Plots of log σ (surface protonic conductivity) vs log p_{H_2O} of both CeO_2 samples in N_2 at 400 °C (a) and 100 °C (b).

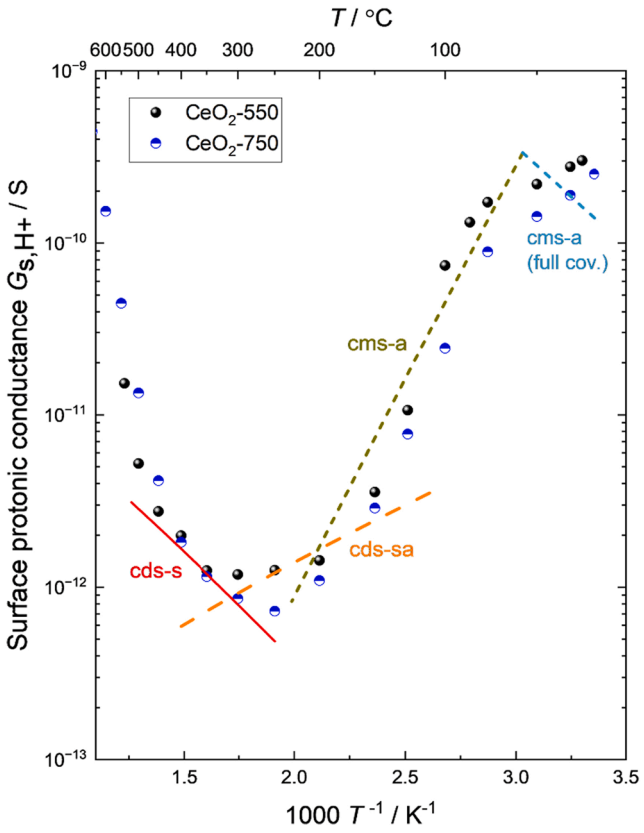

Fig. 8. Surface protonic conductance of the CeO_2 samples at $p_{H_2O} = 0.025$ atm vs $1/T$ in N_2, obtained from the sample conductivities via the BLM (see SI 5.2). The lines are drawn using preexponentials derived for models cds-s, cds-ca, and cms-a in the cases of low coverage, the latter with an extension also to full coverage, as derived below and in SI 5.3. The enthalpies are chosen to fit the experimental data reasonably in different regions as discussed for each model, see SI 5 Table S4.

protonic conduction over CeO_2 surfaces in wet and other hydrogen-containing atmospheres.

Molecular adsorption of water and dissociation of protons to surface oxide ions is described through Eqs. (6)–(14). TG data suggested that the adsorption is not complete (low coverage) and that dissociation prevails at the highest temperatures, but for the concentration of charged species, the mathematics remains the same irrespective of degree of dissociation.

We first consider migration of protons between surface oxide ions, which we may write mechanistically as

$$OH^{\bullet}_{O_s} + O^{x}_{O_s} \rightleftharpoons O^{x}_{O_s} + OH^{\bullet}_{O_s} \tag{16}$$

and which in our case gives rise to a model abbreviated **cds-s** (from **c**hemisorption **d**issociative to **s**urface – with migration on the **s**urface). It will have a relatively high activation energy and prevail at high temperatures with low coverages (few other options for migration). The surface conductance is given by the charge, surface concentration, and charge mobility of the chosen carrier (see ref. [23] and SI 4) and is for the cds-s model

$$G_{s,H^+_{cds\text{-}s}} = F\gamma_{OH^{\bullet}_{O_s}} u_{H^+} = F\gamma_{OH^{\bullet}_{O_s}} X_{O^{x}_{O_s}} u_{H^+0} \frac{1}{T} exp\left(\frac{-\Delta H_{m,H^+_s}}{RT}\right) \tag{17}$$

For low coverage, unprotonated surface oxide ions are generally available, $X_{O^{x}_{Os}} \approx 1$, and by inserting Eq. (14) we get

$$G_{s,H^+_{cds\text{-}s}} = F\gamma_{M_s}\sqrt{2K_{a_{cs}}\frac{p_{H_2O}}{p^0}} u_{H^+0}\frac{1}{T} exp\left(\frac{-\Delta H_{m,H^+_s}}{RT}\right) \tag{18}$$

which we may express as

$$G_{s,H^+_{cds\text{-}s}} = G_{s,H^+_{cds\text{-}s}0}\frac{1}{T} exp\left(\frac{-\left(\frac{1}{2}\Delta H^0_{a_{cm}} + \frac{1}{2}\Delta H^0_{d_{cs}} + \Delta H_{m,H^+_s}\right)}{RT}\right) \tag{19}$$

with preexponential

$$G_{s,H^+_{cds\text{-}s}0} = G^0_{s,H^+_{cds\text{-}s}0}\sqrt{\frac{p_{H_2O}}{p^0}} = \sqrt{2}F\gamma_{M_s} exp\left(\frac{\frac{1}{2}\Delta S^0_{a_{cm}} + \frac{1}{2}\Delta S^0_{d_{cs}}}{R}\right) u_{H^+0}\sqrt{\frac{p_{H_2O}}{p^0}} \tag{20}$$

As detailed in SI 5.3, we estimate preexponentials by assuming $\Delta S_{a_{cm}}{}^0 = -109$ J mol^{-1} K^{-1} as measured for the entropy of condensation of water at 100 °C, [55] $\Delta S_{d_{cs}}{}^0 = 0$ J mol^{-1} K^{-1}, $\gamma_{M_s} \approx 5$ /nm^2 = 8•10^{-10} mol cm^{-2}, and $u_{H^+0} \approx 10$ cm^{2}K V^{-1} s^{-1}, and get $G_{s,\,H^+_{cds\text{-}s}}{}^0 \approx 1.6\bullet10^{-6}$ SK for $p_{H_2O} = 1$ bar and $G_{s,H^+_{cds\text{-}s}0} \approx 2\bullet10^{-7}$ SK at $p_{H_2O} = 0.025$ atm, see entries for the cds-s model in Table S4. In order to make a first estimate of the activation enthalpy of conductance we assume as before $\Delta H_{a_{cm}}{}^0 = -60$ kJ mol^{-1} [36] and $\Delta H_{d_{cs}}{}^0 \approx 20$ kJ mol^{-1}, [46] and if we take $\Delta H_{m,H^+_s} \approx 50$ kJ mol^{-1} as a round value first guess based on the enthalpy of bulk mobility of protons in 50 mol% La-substituted CeO_2 ($La_2Ce_2O_7$) reported as 43 kJ mol^{-1}, [4] we obtain $\Delta H_{c_{cds\text{-}s}} = \frac{1}{2}\Delta H^0_{a_{cm}} + \frac{1}{2}\Delta H^0_{d_{cs}} + \Delta H_{m,H^+_s} \approx +30$ kJ mol^{-1}. The line for this cds-s model in Fig. 8 is drawn to rationalise surface conductance in the region 500–300 °C using the derived preexponential and $\Delta H_{c_{cds\text{-}s}} = +29$ kJ mol^{-1}. Moreover, the $p_{H_2O}^{1/2}$ dependence of the cds-s model is confirmed by the data for 400 °C in Fig. 7 (a).

At the highest p_{H_2O} at 400 °C, the p_{H_2O} dependences in Fig. 7(a) start to increase and as temperature decreases, the conductance levels out in Fig. 8. Both indicate that as *RH* and coverage increases, there is an increasing role of adsorbed species in the conduction process, leading to the next mechanism, where protons jump between **s**urface oxide ions and dissociated **a**dsorbed OH^- groups, hence abbreviated **cds-sa** and representing the reverse of the dissociation to the surface:

$$OH^{\bullet}_{O_s} + M_{M_s}OH^{/} \rightleftharpoons O^{x}_{O_s} + M_{M_s}OH^{x}_{2} \tag{21}$$

The surface protonic conductance along this mechanism can be expressed in terms of the surface protons and will then be proportional to the site fraction of available dissociated adsorbed hydroxide ions:

$$G_{s,H^+_{cds\text{-}sa}} = F\gamma_{OH^{\bullet}_{O_s}} u_{H^+_{sa}} = F\gamma_{OH^{\bullet}_{O_s}} X_{M_{M_s}OH^{/}} u_{H^+0}\frac{1}{T} exp\left(\frac{-\Delta H_{m,H^+_{sa}}}{RT}\right) \tag{22}$$

By assuming low coverage and inserting Eq. (14) we get

$$G_{s,H^+_{cms\text{-}sa}} = 2FK_{a_{cm}}K_{d_{cs}}\gamma_{M_s}\frac{p_{H_2O}}{p^0}u_{H^+0}\frac{1}{T} exp\left(\frac{-\Delta H_{m,H^+_{sa}}}{RT}\right) \tag{23}$$

and hence

$$G_{s,H^+_{cms\text{-}sa}} = G_{s,H^+_{cms\text{-}sa}0}\frac{1}{T} exp\left(\frac{-\left(\Delta H^0_{a_{cm}} + \Delta H^0_{d_{cs}} + \Delta H_{m,H^+_{sa}}\right)}{RT}\right) \tag{24}$$

with preexponential

$$G_{s,H^+_{cms\text{-}sa}0} = G^0_{s,H^+_{cms\text{-}sa}0}\frac{p_{H_2O}}{p^0} = 2F\gamma_{M_s} exp\left(\frac{\Delta S^0_{a_{cm}} + \Delta S^0_{d_{cs}}}{R}\right) u_{H^+0}\frac{p_{H_2O}}{p^0} \tag{25}$$

With assumptions like before we get $G_{s,\,H^+_{cms\text{-}sa}}{}^0 \approx 3\bullet10^{-9}$ SK and $G_{s,H^+_{cms\text{-}sa}0} \approx 8\bullet10^{-11}$ SK at $p_{H_2O} = 0.025$ bar. We assume that migration of protons is easier between these species than solely along the surface, and with the choice of a lower enthalpy of migration of this mechanism of 40 kJ mol^{-1}, we obtain $\Delta H_{c_{cms\text{-}sa}} = \Delta H^0_{a_{cm}} + \Delta H^0_{d_{cs}} + \Delta H_{m,H^+_{sa}}$ to be around 0 kJ mol^{-1}. This conductance is plotted with −10 kJ mol^{-1} in Fig. 8 to

represent the shallow minimum level at 300–200 °C. The model proposes a proportionality to $p_{H_2O}^{1}$ of surface protonic conduction, which is approached for high p_{H_2O} at 400 °C in our measurements (Fig. 7 a) and in those of Manabe et al. [51]

As we go lower in temperature, the conductance starts to increase more steeply in Fig. 8, and the p_{H_2O} dependence increases further, see Fig. 7 (b). This suggests even more involvement of adsorbed species for migration: We consider that dissociation still goes to surface oxide ions, but may be weaker as its enthalpy is positive and temperature is now lower. Migration now takes place between the remaining adsorbed water molecules and dissociated hydroxide ions, hence the mechanism is abbreviated **cds-a** or **cms-a** depending on degree of dissociation, and migration proceeds according to

$$M_{M_s}OH_2^x + M_{M_s}OH^{/} \rightleftharpoons M_{M_s}OH^{/} + M_{M_s}OH_2^x \quad (26)$$

For this mechanism we realise that dissociation is needed, but that also some undissociated water needs to remain. We will see how it comes out in the thermodynamics. The surface conductance can in this case be written

$$\begin{aligned} G_{s,H^+_{cds-a}} &= G_{s,H^+_{cms-a}} = F\gamma_{M_{M_s}OH_2^x} u_{H^+_a} \\ &= F\gamma_{M_{M_s}OH_2^x} \frac{\gamma_{M_{M_s}OH^{/}}}{\gamma_{M_s}} u_{H^+0} \frac{1}{T} exp\left(\frac{-\Delta H_{m,H^+_a}}{RT}\right) \end{aligned} \quad (27)$$

which, under assumption of **low coverage** by combination with Eq. (7) and Eq. (12) yields

$$G_{s,H^+_{cms-a}} = F\gamma_{M_s} K_{a_{cm}} \sqrt{2K_{a_{cds}}} \left(\frac{p_{H_2O}}{p^0}\right)^{3/2} u_{H^+0} \frac{1}{T} exp\left(\frac{-\Delta H_{m,H^+_a}}{RT}\right) \quad (28)$$

We rewrite this as

$$\begin{aligned} G_{s,H^+_{cms-a}} &= G_{s,H^+_{cms-a}0} \frac{1}{T} exp\left(\frac{-\Delta H_{c_{cms-a}}}{RT}\right) \\ &= G_{s,H^+_{cms-a}0} \frac{1}{T} exp\left(\frac{-\left(\Delta H^0_{a_{cm}} + \frac{1}{2}\Delta H^0_{a_{cds}} + \Delta H_{m,H^+_a}\right)}{RT}\right) \end{aligned} \quad (29)$$

with $\Delta H_{c_{cms-a}} = \Delta H^0_{a_{cm}} + \frac{1}{2}\Delta H^0_{a_{cds}} + \Delta H_{m,H^+_a} = \frac{3}{2}\Delta H^0_{a_{cm}} + \frac{1}{2}\Delta H^0_{d_{cs}} + \Delta H_{m,H^+_a}$, and preexponential

$$\begin{aligned} G_{s,H^+_{cms-a}0} &= G^0_{s,H^+_{cms-a}0} \left(\frac{p_{H_2O}}{p^0}\right)^{3/2} \\ &= \sqrt{2}F\gamma_{M_s} exp\left(\frac{\frac{3}{2}\Delta S^0_{a_{cm}} + \frac{1}{2}\Delta S^0_{d_{cs}}}{R}\right) u_{H^+0} \left(\frac{p_{H_2O}}{p^0}\right)^{3/2} \end{aligned} \quad (30)$$

As indicated above, the adsorption comes in at full play, while the dissociation has a two-sided effect and comes in to a lesser extent. With assumptions as before, we obtain $G_{s,H^+_{chm-a}}{}^0 \approx 3\bullet10^{-12}$ SK and $G_{s,H^+_{chm-a}0} \approx 1\bullet10^{-14}$ SK at p_{H_2O}= 0.025 bar. If we now take the mobility in the molecular layer to be lower, at 20 kJ mol^{-1}, the enthalpy of conduction may be estimated to be $\Delta H_{c_{cms-a}} = \frac{3}{2}\Delta H^0_{a_{cm}} + \frac{1}{2}\Delta H^0_{d_{cs}} + \Delta H_{m,H^+_a} \approx -60$ kJ mol^{-1}, meaning that conductance increases strongly with decreasing temperature, describing roughly the conductivity in the range 200–100 °C in Fig. 8, there plotted with $\Delta H_{c_{cms-a}} = -45$ kJ mol^{-1}. This behaviour of transport in the chemisorbed layer hence fits the conductivity in the region where it earlier has traditionally been assigned to transport in the physisorbed layer. Moreover, the predicted $p_{H_2O}^{3/2}$ dependence fits well with the data for 100 °C in Fig. 7 (b), further supporting the assigned mechanism.

As before, it does not matter mathematically whether we consider a mainly undissociated (cms-a) or dissociated (cds-a) case as long as we have low coverage. The difference becomes evident, however, if we consider the full coverage cases. As we pass below 100 °C, the conductivities in Fig. 8 level off with decreasing temperature, which is only rational if we approach full coverage. We did indeed see a conductivity decreasing with decreasing temperature near room temperature for one sample (see SI 4.2, Fig. S7). These behaviours must follow one of the models for full coverage derived in SI 5.3. In the dissociated cds-a case, we predict an enthalpy of conduction close to 0 kJ mol^{-1}, which with the predicted preexponential cannot fit the levelling off at low temperatures in Fig. 8. However, the case of low dissociation and full coverage can: At full coverage, $\gamma_{M_{M_s}OH_2^x} \approx \gamma_{M_s}$, and low dissociation ($\gamma_{O_s} \approx 2\gamma_{M_s}$), the conductance becomes

$$G_{s,H^+_{cms-a}} = F\gamma_{M_{M_s}OH_2^x} u_{H^+_a} = F\gamma_{M_s}\sqrt{2K_{d_{cs}}} u_{H^+0} \frac{1}{T} exp\left(\frac{-\Delta H_{m,H^+_a}}{RT}\right) \quad (31)$$

which we rewrite as

$$\begin{aligned} G_{s,H^+_{cms-a}} &= G_{s,H^+_{cms-a}0} \frac{1}{T} exp\left(\frac{-\Delta H_{cms-a}}{RT}\right) \\ &= G_{s,H^+_{cms-a}0} \frac{1}{T} exp\left(\frac{-\left(\frac{1}{2}\Delta H^0_{d_{cs}} + \Delta H_{m,H^+_a}\right)}{RT}\right) \end{aligned} \quad (32)$$

with preexponential

$$G_{s,H^+_{cms-a}0} = G^0_{s,H^+_{cms-a}0} = \sqrt{2}F\gamma_{M_s} exp\left(\frac{\frac{1}{2}\Delta S^0_{d_{cs}}}{R}\right) u_{H^+0} \quad (33)$$

coming out as $G_{s,H^+_{cms-a}0} = G^0_{s,H^+_{cms-a}0} = 1.1\bullet10^{-3}$ SK. If the activation enthalpy of mobility is still 20 kJ mol^{-1}, the enthalpy of conduction may be estimated to be around +30 kJ mol^{-1}. It is plotted in Fig. 8 with $\Delta H_{c_{cms-a}}$= + 25 kJ mol^{-1} as a continuation to lower temperatures where it takes over for the low coverage model.

The SI 5.3 also evaluates dissociation within the chemisorbed layer itself, to form adsorbed OH^- and H_3O^+ ions. This corresponding cma-a mechanism corresponds to one proposed by Raz et al. [9] and predicts conductances and temperature behaviours similar to those of the cms-a and cds-a models above. However, we must expect that dissociation to the surface is stronger (has a lower enthalpy) than within the adsorbed water layer, and by that the H_3O^+ ions will be minority defects in the overall electroneutrality and play little role.

3.5.3. Conduction in physisorbed water

For most samples, including the ones in Fig. 8, the continuing increase in conductivity at the lowest temperatures suggests the onset of conduction in the physisorbed layers that are filling up under these conditions. Fig. 9 shows examples of p_{H_2O}dependences of conductivity at 25 °C (RT), where we believe that physisorbed water starts to contribute. The CeO_2–550 sample lost all conductivity at $RH < 30\%$, but otherwise, both samples showed conductivities approximately proportional to p_{H_2O} at $RH < 60\%$, while the p_{H_2O} dependences increased to at least $p_{H_2O}^2$ at $RH > 60\%$. We cannot attribute these behaviours to quantitative models like we did above for the chemisorbed water and for physisorbed water in our previous work on ZrO_2. Qualitatively, it may reflect hysteresis in the contact angle and wettability of liquid-like physisorbed water and that the activation enthalpy of the mobility of protons decreases with increasing thickness and decreasing viscosity of the liquid-like physisorbed water layer.

For a CeO_2–550 sample that was heated to 540 °C in dry N_2 and then cooled straight to RT, the conductivity was initially immeasurably small in dry atmosphere. It remained so upon small steps towards wetter conditions, and became measurable only above $RH \approx 30\%$, and took several days to equilibrate. We suggest that this relates to a restructuring of the CeO_2 surface upon beginning adsorption of water in order to lower the surface energy. After completion of this process, changes in humidity were equilibrated faster, within a couple of hours. Combined ^{17}O and ^{1}H

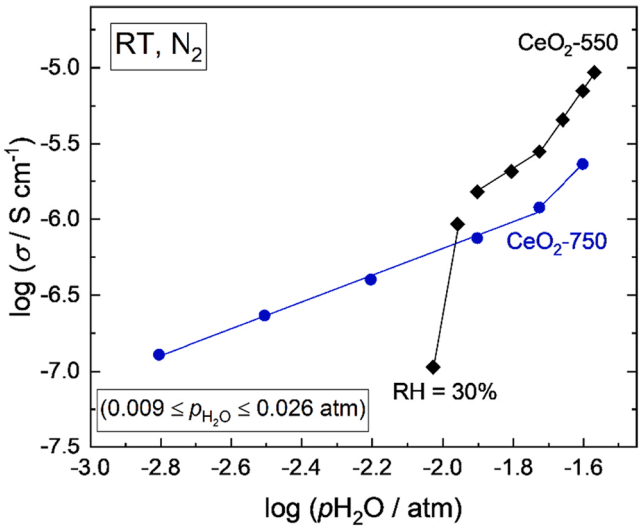

Fig. 9. p_{H_2O}dependence of surface protonic conductivity at 25 °C (RT) for both CeO_2 samples.

solid-state NMR spectroscopy with DFT calculations indicate that reconstructions occur on CeO_2{100}nanotube surfaces upon adsorption of water. [56] Yang et al. [57] provided direct spectroscopic evidence for the extensive restructuring of rod-shaped ceria nanoparticles, and they further showed that {111} nanofacets is an intrinsic property of the catalytically most active CeO_2{110} surface. For the CeO_2–750 sample, long equilibration times of the order of 24 h were required to reach steady-state conditions at each *RH* level at RT. Similarly, Simons et al. [24] reported that hydration of ceria took up to three days for thin films at RT.

All in all, the behaviours of adsorption and conduction in physisorbed water layers on nano-ceria at high *RH* appear to be a result of hydrophobicity and restructuring of the surface, maybe involving changes in surface composition (degree of hydrogenation). We may also anticipate that competing impurity adsorbents such as CO_2 and hydrocarbons may play a role. [58] Moreover, the average pore diameters of ~12 nm for CeO_2–550 and ~ 20 nm for CeO_2–750 from BET analysis (SI 6, Fig. S13) suggest capillary condensation of water close to RT, which still may not be reflected in the measured conductivity of CeO_2 because the hydrophobicity prevents connection of the narrowest parts of the pores. Furthermore, wedge-shaped porosity due to low-temperature sintering of nanocrystalline materials can also add favourable water adsorption sites. [19]

3.6. Comparison with recent studies of ZrO_2 and TiO_2

Recent literature on surface protonics of monoclinic ZrO_2 by Sun et al. [23] and anatase TiO_2 by Kang et al. [22] with similar microstructures and methodologies invites comparisons in view of the new developments in the present paper on CeO_2. The surface conductance by protons from chemisorbed water over surface oxide ions (cds-s) that dominates at 300–400 °C appears comparable for these oxides when microstructure is taken into account via the BLM. The enthalpies are similar, and delineation of adsorption and proton mobility is difficult because of insufficient literature data and unreliable subtraction of the competing native (dry) conduction.

At intermediate temperatures (200–300 °C), poorly faceted ZrO_2 and {101}-dominated TiO_2 have considerable conduction across a shallow minimum in common with CeO_2, which we here for the first time has given a possible interpretation in terms of proton transport between surface oxide and adsorbed hydroxide species (cds-sa). Future studies must validate this and investigate whether and why certain oxides and surfaces promote this mechanism.

Kang et al. [22] found by in situ FTIR that anatase TiO_2 had physisorbed water below 200 °C, and the conductance especially of samples grown with predominantly {100} and {001} facets had more negative enthalpies and higher levels of surface protonic conductivity than in our CeO_2. Below 100 °C the conduction in TiO_2 increased even more strongly with decreasing temperature, assigned to liquid-like physisorbed water, in stark contrast to the behaviour of the hydrophobic CeO_2. All in all, TiO_2 appears to have stronger adsorption of water and to be hydrophilic contrary to the hydrophobic CeO_2. It seems that ZrO_2 behaves somewhere between TiO_2 and CeO_2 in terms of activation enthalpy and hydrophilicity and the contribution from liquid-like physisorbed water, depending on the degree of faceting of the surfaces.

More dedicated p_{H_2O} dependences of TG and conductivity data for other oxides like we have taken here will help discriminate mechanisms and allow more reliable comparative parameterisation.

4. Conclusions

Water adsorption and surface protonic conductivity measurements on nominally pure porous sintered CeO_2 samples confirm the expectancy that adsorption relates to specific surface area, while surface conductivity relates to grain size and porosity, quantifiable through a brick layer model. Thermogravimetry supports indications in the literature that the surface and/or subsurface of CeO_2 in presence of water vapour is hydrogenated to Ce^{3+} ions and protons H^+, that the following chemisorption is dissociative at high temperatures, and that physisorption sets in only at the highest relative humidities, typical of hydrophobic behaviour.

The observed dual time constants in the high frequency part of the impedance spectra represent according to our interpretation conduction over the concave and the convex part of curved surfaces. This together with the absence of an electrode impedance under dry atmospheres suggests that the native conductivity is surface electronic, likely from the hydrogenated layer. The conductivity under wet atmosphere below 500 °C is dominated entirely by surface protonic conduction.

The preexponentials and p_{H_2O} dependences of surface protonic conductivity are discussed on the basis of models for adsorption and dissociation of water and migration of protons, which connect the predicted surface protonic conductances to measured conductivity of the sample via the brick layer model. In the absence of physisorbed water, we have expanded models for transport from and in chemisorbed water to comprise migration of protons between surface oxide ions, migration between surface oxide ions and adsorbed hydroxide ions, and migration between adsorbed water molecules and hydroxide ions, with predicted positive, near-zero, and apparent negative activation enthalpies of conduction, respectively, and $p_{H_2O}^{1/2}$, $p_{H_2O}^{1}$, and $p_{H_2O}^{3/2}$ dependences. With predicted pre-exponentials and estimates of enthalpies for adsorption, dissociation, and proton diffusion, these match observed surface protonic conductances at high, intermediate, and low temperatures. For hydrophobic CeO_2, the low temperature mechanism of proton transport between adsorbed species behaves similarly as what is traditionally concluded to reflect physisorbed water in other, hydrophilic oxides, where probably the two contribute together.

At the highest *RH*s, the surface protonic conductivity of CeO_2 levels off, as expected from saturation to full coverage of the chemisorbed layer. A contribution from physisorbed water sets in, but remains modest and suffers from hysteresis of wetting and maybe restructuring of the surface and surface-oxide interface.

The TG data of dissociative chemisorption fit literature suggestions of a standard molecular adsorption enthalpy of −60 kJ mol^{-1} H_2O and dissociation of a proton to a surface oxide ion of the order of +20 kJ mol^{-1} H_2O. With these, conductivity data further suggest that migration of protons between surface oxide ions have activation energies as high as 50 kJ mol^{-1}, while they decrease towards values around 20 kJ mol^{-1} in the adsorbed layer.

It is believed that the findings have consequences for understanding

and controlling the surface properties of ceria-based nanomaterials. This study further suggests that incomplete and weak yet dissociative chemisorption of water may plays an important role for ceria as a catalyst in that much of the surface is left available for reactant molecules, while dissociated mobile protons are available on the surface along with electrons from the Ce^{3+} in the surface.

The deeper analysis of hydrogenation of the surface, and of the properties of the hydrogenated layer is suggested for future studies, as are the consequences for details of the models presented here for transport in the chemisorbed water layer.

Declaration of Competing Interest

The authors declare no existing conflict of interest.

Data availability

Data will be made available on request.

Acknowledgements

X.S., A.C, and T.N. acknowledge MoZEES, a Norwegian Centre for Environment-Friendly Energy Research (FME), co-sponsored by The Research Council of Norway (project #257653) and 40 partners from research, industry and public sector. X.S., E.V., P.M.R., and T.N. acknowledge the SUPROX project (#280868) financed by the Research Council of Norway. S.P. acknowledges the iCSI project (#237922) financed by the Research Council of Norway. The authors thank Dr. David S. Wragg (University of Oslo) for HT-XRD measurements.

Appendix A. Supplementary data

Supplementary data to this article can be found online at https://doi.org/10.1016/j.apsusc.2022.155590.

References

[1] M.F. Liu, et al., An efficient SOFC based on Samaria-doped ceria (SDC) electrolyte, J. Electrochem. Soc. 159 (6) (2012) B661–B665.
[2] N. Jaiswal, et al., A brief review on ceria based solid electrolytes for solid oxide fuel cells, J. Alloys Compd. 781 (2019) 984–1005.
[3] Y. Nigara, et al., Hydrogen permeability in $(CeO_2)_{0.9}(GdO_{1.5})_{0.1}$ at high temperatures, Solid State Ionics 159 (1–2) (2003) 135–141.
[4] L.E. Kalland, et al., Structure, hydration, and proton conductivity in 50% La and Nd doped CeO_2 - $La_2Ce_2O_7$ and $Nd_2Ce_2O_7$ - and their solid solutions, Solid State Ionics 354 (2020).
[5] R. Sato, et al., Proton migration on hydrated surface of cubic ZrO_2: ab initio molecular dynamics simulation, J. Phys. Chem. C 119 (52) (2015) 28925–28933.
[6] S.Ø. Stub, E. Vøllestad, T. Norby, Mechanisms of protonic surface transport in porous oxides: example of YSZ, J. Phys. Chem. C 121 (23) (2017) 12817–12825.
[7] S.Ø. Stub, E. Vøllestad, T. Norby, Protonic surface conduction controlled by space charge of intersecting grain boundaries in porous ceramics, J. Mater. Chem. A 6 (18) (2018) 8265–8270.
[8] B. Scherrer, et al., On proton conductivity in porous and dense Yttria stabilized zirconia at low temperature, Adv. Funct. Mater. 23 (15) (2013) 1957–1964.
[9] S. Raz, et al., Characterization of adsorbed water layers on Y_2O_3-doped ZrO_2, Solid State Ionics 143 (2) (2001) 181–204.
[10] E.M. Kock, et al., Structural and electrochemical properties of Physisorbed and chemisorbed water layers on the ceramic oxides Y_2O_3, YSZ, and ZrO_2, ACS Appl. Mater. Interfaces 8 (25) (2016) 16428–16443.
[11] J. Gao, et al., Insights into the proton transport mechanism in TiO_2 simple oxides by in situ Raman spectroscopy, ACS Appl. Mater. Interfaces 12 (34) (2020) 38012–38018.
[12] S.Ø. Stub, et al., The influence of acceptor and donor doping on the protonic surface conduction of TiO_2, Phys. Chem. Chem. Phys. 20 (23) (2018) 15653–15660.
[13] F. Maglia, et al., Low temperature proton conduction in bulk nanometric TiO_2 prepared by high-pressure field assisted sintering, J. Mater. Res. 27 (15) (2012) 1975–1981.
[14] M.T. Colomer, F. Rubio, J.R. Jurado, Transport properties of fast proton conducting mesoporous silica xerogels, J. Power Sources 167 (1) (2007) 53–57.
[15] S. Kim, et al., On the conduction pathway for protons in nanocrystalline yttria-stabilized zirconia, Phys. Chem. Chem. Phys. 11 (17) (2009) 3035–3038.
[16] H.J. Avila-Paredes, et al., Grain boundaries in dense nanocrystalline ceria ceramics: exclusive pathways for proton conduction at room temperature, J. Mater. Chem. 20 (45) (2010) 10110–10112.
[17] S. Kim, et al., Unprecedented room-temperature electrical power generation using nanoscale fluorite-structured oxide electrolytes, Adv. Mater. 20 (3) (2008) 556–559.
[18] D. Perez-Coll, E. Sanchez-Lopez, G.C. Mather, Influence of porosity on the bulk and grain-boundary electrical properties of Gd-doped ceria, Solid State Ionics 181 (21–22) (2010) 1033–1042.
[19] M. Shirpour, et al., On the proton conductivity in pure and gadolinium doped nanocrystalline cerium oxide, Phys. Chem. Chem. Phys. 13 (3) (2011) 937–940.
[20] G. Gregori, M. Shirpour, J. Maier, Proton conduction in dense and porous Nanocrystalline ceria thin films, Adv. Funct. Mater. 23 (47) (2013) 5861–5867.
[21] E.L. Runnerstrom, et al., Colloidal nanocrystal films reveal the mechanism for intermediate temperature proton conductivity in porous ceramics, J. Phys. Chem. C 122 (25) (2018) 13624–13635.
[22] X.L. Kang, et al., Facet-engineered TiO_2 nanomaterials reveal the role of water-oxide interactions in surface protonic conduction, J. Mater. Chem. A 10 (1) (2022) 218–227.
[23] X.W. Sun, et al., Quantifiable models for surface protonic conductivity in porous oxides - case of monoclinic ZrO_2, Phys. Chem. Chem. Phys. 24 (2022) 11856–11871.
[24] P. Simons, K.P. Torres, J.L.M. Rupp, Careful choices in low temperature ceramic processing and slow hydration kinetics can affect proton conduction in ceria, Adv. Funct. Mater. 31 (31) (2021) 2009630.
[25] Y. Hisai, et al., Enhanced activity of catalysts on substrates with surface protonic current in an electrical field - a review, Chem. Commun. 57 (47) (2021) 5737–5749.
[26] K.B. Zhou, et al., Enhanced catalytic activity of ceria nanorods from well-defined reactive crystal planes, J. Catal. 229 (1) (2005) 206–212.
[27] A. Trovarelli, J. Llorca, Ceria catalysts at nanoscale: how do crystal shapes shape catalysis? ACS Catal. 7 (7) (2017) 4716–4735.
[28] A. Thøgersen, et al., In-situ electron loss spectroscopy reveals surface dehydrogenation of hydrated ceria nanoparticles at elevated temperatures, J. Phys. Chem. Solids 170 (2022), 110955.
[29] J. Paier, C. Penschke, J. Sauer, Oxygen defects and surface chemistry of ceria: quantum chemical studies compared to experiment, Chem. Rev. 113 (6) (2013) 3949–3985.
[30] D.R. Mullins, The surface chemistry of cerium oxide, Surf. Sci. Rep. 70 (1) (2015) 42–85.
[31] M. Mogensen, N.M. Sammes, G.A. Tompsett, Physical, chemical and electrochemical properties of pure and doped ceria, Solid State Ionics 129 (1–4) (2000) 63–94.
[32] G.C. Shearer, et al., Defect engineering: tuning the porosity and composition of the metal-organic framework UiO-66 via modulated synthesis, Chem. Mater. 28 (11) (2016) 3749–3761.
[33] G.N. Kalantzopoulos, et al., Factors determining microporous material stability in water: the curious case of SAPO-37, Chem. Mater. 32 (4) (2020) 1495–1505.
[34] K.S.W. Sing, et al., Reporting Physisorption data for gas solid systems with special reference to the determination of surface-area and porosity (recommendations 1984), Pure Appl. Chem. 57 (4) (1985) 603–619.
[35] A.V. Radha, et al., Surface enthalpy, enthalpy of water adsorption, and phase stability in Nanocrystalline monoclinic zirconia, J. Am. Ceram. Soc. 92 (1) (2009) 133–140.
[36] S. Hayun, T.Y. Shvareva, A. Navrotsky, Nanoceria - energetics of surfaces, interfaces and water adsorption, J. Am. Ceram. Soc. 94 (11) (2011) 3992–3999.
[37] G.C.C. Costa, et al., Calorimetric measurement of surface and Interface enthalpies of Yttria-stabilized zirconia (YSZ), Chem. Mater. 22 (9) (2010) 2937–2945.
[38] J. Canivet, et al., Structure-property relationships of water adsorption in metal-organic frameworks, New J. Chem. 38 (7) (2014) 3102–3111.
[39] M. Fronzi, M.H.N. Assadi, D.A.H. Hanaor, Theoretical insights into the hydrophobicity of low index CeO_2 surfaces, Appl. Surf. Sci. 478 (2019) 68–74.
[40] G. Azimi, et al., Hydrophobicity of rare-earth oxide ceramics, Nat. Mater. 12 (4) (2013) 315–320.
[41] S.L. Wachowski, et al., Structure and water uptake in BaLnCo2O6− δ (ln= La, Pr, Nd, Sm, Gd, Tb and Dy), Acta Mater. 199 (2020) 297–310.
[42] P.Z.G. Schuster, C. Sandorfy, The Hydrogen Bond: Recent Developments in Theory and Experiments III: Dynamics, thermodynamics and special systems. Chapter 27: Hydrogen Bonds in Systems of Adsorbed Molecules, North-Holland Publishing Company, Amsterdam, New York, Oxford, 1976, p. 1263. H. Knözinger, Editor.
[43] S.V.N.T. Kuchibhatla, et al., An unexpected phase transformation of ceria nanoparticles in aqueous media, J. Mater. Res. 34 (3) (2019) 465–473.
[44] M. Fronzi, et al., Water adsorption on the stoichiometric and reduced CeO2(111) surface: a first-principles investigation, Phys. Chem. Chem. Phys. 11 (40) (2009) 9188–9199.
[45] S. Kumar, P.K. Schelling, Density functional theory study of water adsorption at reduced and stoichiometric ceria (111) surfaces, J. Chem. Phys. 125 (20) (2006) 204704.
[46] M.A. Blesa, A.J.G. Maroto, A.E. Regazzoni, Surface-acidity of metal-oxides immersed in water - a critical analysis of thermodynamic data, J. Colloid Interface Sci. 140 (1) (1990) 287–290.
[47] A. Tschope, E. Sommer, R. Birringer, Grain size-dependent electrical conductivity of polycrystalline cerium oxide I. Experiments, Solid State Ionics 139 (3–4) (2001) 255–265.

[48] P. Knauth, et al., Study of compaction and sintering of nanosized oxide powders by in situ electrical measurements and dilatometry: Nano CeO_2—case study, J. Electroceram. 34 (1) (2015) 82–90.
[49] M.C. Gobel, et al., Boundary effects on the electrical conductivity of pure and doped cerium oxide thin films, Phys. Chem. Chem. Phys. 12 (42) (2010) 14351–14361.
[50] T.S. Oh, et al., Proton conductivity of columnar ceria thin-films grown by chemical vapor deposition, Phys. Chem. Chem. Phys. 15 (7) (2013) 2466–2472.
[51] R. Manabe, et al., Evaluating surface protonic transport on cerium oxide via electrochemical impedance spectroscopy measurement, Solid State Commun. 270 (2018) 45–49.
[52] S. Miyoshi, et al., Water uptake and conduction property of nano-grained yttria-doped zirconia fabricated by ultra-high pressure compaction at room temperature, Solid State Ionics 207 (2012) 21–28.
[53] E. Ruiz-Trejo, J.A. Kilner, Possible proton conduction in $Ce_{0.9}Gd_{0.1}O_{2\text{-delta}}$ nanoceramics, J. Appl. Electrochem. 39 (4) (2009) 523–528.
[54] W. Sun, et al., Investigation on proton conductivity of $La_2Ce_2O_7$ in wet atmosphere: dependence on water vapor partial pressure, Fuel Cells 12 (3) (2012) 457–463.
[55] W. Wagner, A. Pruß, The IAPWS formulation 1995 for the thermodynamic properties of ordinary water substance for general and scientific use, J. Phys. Chem. Ref. Data 31 (2) (2002) 387–535.
[56] J.C. Chen, et al., Polar surface structure of oxide nanocrystals revealed with solid-state NMR spectroscopy, Nat. Commun. 10 (2019), 5420.
[57] C.W. Yang, et al., Surface faceting and reconstruction of ceria nanoparticles, Angewandte Chemie-International Edition 56 (1) (2017) 375–379.
[58] E. Kulah, et al., Surface chemistry of rare-earth oxide surfaces at ambient conditions: reactions with water and hydrocarbons, Sci. Rep. 7 (2017) 43369.